frontiers | Frontiers in Physics

TYPE Original Research
PUBLISHED 30 May 2025
DOI 10.3389/fphy.2025.1586858

OPEN ACCESS

EDITED BY
Xue Jiang,
Fudan University, China

REVIEWED BY
Chen Shen,
Rowan University, United States
Hy Long,
Nanjing University, China

*CORRESPONDENCE
Yu Fang,
fangyuhust@163.com

RECEIVED 03 March 2025
ACCEPTED 15 May 2025
PUBLISHED 30 May 2025

CITATION
Xu Z-x, Fang Y and Wang X-p (2025) Enhanced fano-type broadband acoustic ventilated silencer with arbitrary geometrical configurations.
Front. Phys. 13:1586858.
doi: 10.3389/fphy.2025.1586858

Enhanced fano-type broadband acoustic ventilated silencer with arbitrary geometrical configurations

Zi-xiang Xu[1], Yu Fang[1]* and Xiao-ping Wang[2]

[1]Nanjing Research Institute of Electronics Technology, Nanjing, China, [2]The Unit 93209 of People's Liberation Army, Beijing, China

The introduction of Fano resonance into acoustic metamaterials provides the possibility for simultaneous airborne sound insulation and high-efficiency ventilation, while the ultranarrow Fano line shape and limited shape configurations restrict the expansion to practical applications. In this work, we theoretically propose and demonstrate a broadband low-frequency ventilation acoustic chiral barrier with arbitrary geometrical configurations, where consecutive multiple Fano resonances (CMFRs) generate destructive interference in the range of 479–1,032 Hz. The barrier unit with a binary planar design is composed of the chiral space-coiling tunnel and hollow pipe, providing the discrete resonant and continuum states for Fano resonant system. By means of judiciously tuning the coupling of the above-mentioned two states, multi-order Fano resonances manifest as low transmission in a wide frequency range. Good agreement between simulated, theoretical, and measured results validates the effectiveness of the proposed barrier in the broad low-frequency range, in which the laminar and turbulent flow models reveal the high air-permeability of our barrier. Thanks to the unit planar profile, we can flexibly customize the arbitrary geometrical configurations of the barrier to extend into three-dimensional (3D) space for practical noise reduction applications. Our research makes it possible to construct ventilation artificial metastructure with a flexible manner for broadband sound attenuation.

KEYWORDS

acoustic, metamateials, silencer, fano resonance, broadband insulating

Introduction

In the field of acoustic metamaterials (AMs), there remains a significant challenge for simultaneous air-borne sound-proofing and airflow permeability [1–3]. In the last decade, AMs based on local resonance have witnessed tremendous progress in ventilation barriers, while the ventilation areas of the structures have been sacrificed to mount silencing metamaterial components. To break the restriction, broadband acoustic barriers based on Fano resonances [4–13] has been introduced in airborne soundproof engineering [14–26] for its high-efficiency ventilation which come from its physical essence of the coupling of unimpeded pathways [27, 28]. However, conventional Fano resonance exhibits as an ultra-sharp asymmetric line [29], which is induced by the equal strength of the discrete resonant state and a smooth continuum state in background media [30], extremely limiting the related applications in actual wideband scenarios with complex frequency components. In pursuit of a broadband sound-proofing yet airflow-permeating performance, the mechanism of acoustic consecutive Fano resonances was presented to broaden the sound insulating bandwidth [31–36]. For example, Xu et al. proposed a low-frequency double-helix meta-silencer to realize broadband sound attenuation and high ventilation. Similar work [36] have emerged recently, however, their bandwidth is still smaller than half an octave due to the fact that the transmission peaks of Fano resonances intuitively limits the superposition of more higher-order Fano resonances [30]. To obtain more broadband performance in a Fano-based ventilation design, the higher-order Fano resonances must come into play. In addition, the previous works [20, 21, 37] in the field of sound insulating metamaterials pay more attention to the development of single metastructure, ignoring the requirements of complex structural configurations in actual application scenarios. Therefore, the mechanism for realizing broader soundproofing frequency range in acoustic Fano systems with simplicity and flexibility so far remains elusive.

In this work, we theoretically propose and numerically demonstrate a broadband low-frequency acoustic chiral barrier enabled by consecutive multiple Fano resonances, dramatically decreasing the incident energy from 479 to 1,032 Hz while maintaining efficient ventilation. The barrier with a planar profile is composed of a binary design of the chiral space coiling tunnel and hollow pipe. Due to reasonable superposition of multi-order Fano resonance modes, the response strength from the discrete and continuum states keeps quasi-balanced, generating high-quality destructive interference in a broadband. Good agreement between the simulated, analytical, and experimental results verifies the effectiveness of our proposal. Our work paves a road for low-frequency airborne soundproof structures in the presence of ventilation.

As shown in Figure 1A, we consider the case of the planar profile of the barrier unit, which schematically illustrates the proposed broadband ventilation chiral barrier composed of an opened pathway and a labyrinthine channel. The incident sound waves are vertically incident along the y-axis from upstream, the incident waves are partitioned into two parts at the upstream interface of the unit and travel forward in the opened region and the space-coiling path separately, and then flow jointly towards the downstream side of the unit. To address impedance mismatch arising from the space-coiling geometry, we strategically employ a variable cross-section space-coiling channel to ensure high transmission efficiency. This design maintains a constant effective refractive index, facilitating Fabry-Perot resonances [38] and enabling the formation of desired resonant modes that support discrete resonant modes for Fano resonance. The term "chiral" refers to the unique geometric configuration of our acoustic meta-unit, which exhibits handedness in its design. This handedness is achieved through the specific arrangement of the space-coiling tunnel and hollow pipe within the unit. The introduction of chirality in our design allows for the manipulation of acoustic waves to achieve enhanced impedance matching and broadband noise reduction. In our proposed meta-unit, formed by combining these two kinds of components together, the interference between the resonant scattering of discrete states and the background scattering of continuous states leads to the desired acoustic performance. The hollow pipe unit, which always allows a unity transmission as long as this unit has a subwavelength size, plays the role of the continuum in Fano resonance. This configuration supports the formation of broadband Fano resonances through the constructive and destructive interference between discrete and continuous states.

Specifically, the height of the space-coiling channel and the open channel along the y-axis is h_1 and h_2 respectively. the structure of the space-coiling channel is symmetrically distributed with N layer on each side. The wall thickness d of the structure is held constant. In addition, the ith channel width $w_i (1 \le i \le N)$ is dictated by the width of the entrance channel w_1 and the common ratio factor p, expressed as $w_i = w_1 \times p^{(1-i)}$, while w_i can be expressible as $w_i = w_1 \times p^{(1-2N)}$. Particularly, to ensure the continuous variation of the cross section of the N^{th} layer channel and the $N+1^{th}$ layer channel, the channel width at the connection matches their width. By this definition, the width w_i for the ith channel coincides with that w_{2N+1-i} for the $2N+1^{th}$ channel, and a structure with $p = 1$ constitutes a space-coiling structure with a uniform cross-sectional dimension. Along the z-axis, the overall height can be arbitrarily tune according to the application scenario. The flexible geometries with various configurations, as illustrated in Figures 1b–d, demonstrate the versatility and adaptability of the designed unit for attaining the targeted performance characteristics.

As shown in Figure 2a, the space-coiling channel keeps high averaged transmission coefficient more than 0.92 in the range of 400–1,200 Hz due to variable cross-section design, which maintain the subsequent high-quality interference with the open channel. The space-coiling channel exhibits a linear phase profile [39], which is indicative of its broadband non-dispersive property. Additionally, it supports consecutive resonances: dipolar resonances at 517 Hz and 1,098 Hz, and a monopolar resonance at 776 Hz. These resonances are characterized by distinct radiation patterns. Specifically, for the dipolar resonances, sound radiates strongly along the axis connecting the two poles, with minimal radiation perpendicular to this axis. In contrast, the monopolar resonance at 776 Hz exhibits a radiation pattern with sound pressure being uniform in both directions. The effective refractive index of the space-coiling channel can be obtained from the simulated results by $n = \frac{\Delta\varphi}{k_0 d}$. However, the ventilation channels only support resonances at higher frequencies and the acoustic pressure is linear in terms of phase change at lower frequencies.

To study acoustic wave transmission and reflection behavior of the acoustic barrier, we introduce a simplified acoustic model of the chiral unit, where the actual space-coiling channel is replaced with a straightened effective channel filled with effective fluid. The effective fluid is characterized by constitutive parameters (ρ_e and c_e) such that the weight of fluid inside the channel and sound travelling time in the two channels are guaranteed identical. The ventilation channels are filled with air (ρ_0 and c_0). An analytical model has been developed by combining the Green's function theory [40] and the transfer matrix method [41]. First, the pressure fields on the downstream and upstream can be expressed as

$$p_t(x,y) = p_d \quad \text{and} \quad p_r(x,y) = P_i e^{ikx} + p_u \tag{1}$$

where p_u and p_d are the radiation fields in the upstream and downstream, respectively, and estimated through the Green's function of the tube

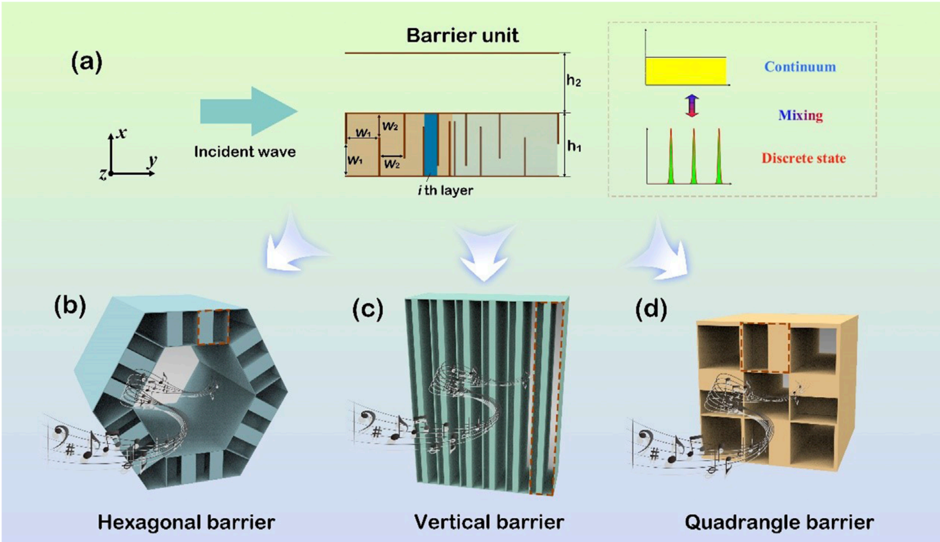

FIGURE 1
Schematic illustration for the designed broadband ventilation barrier. **(a)** The details of the chiral barrier unit and its geometry dimensions on the x-y plane. **(b–d)** The ventilation barrier based on the designed unit with different geometrical configurations.

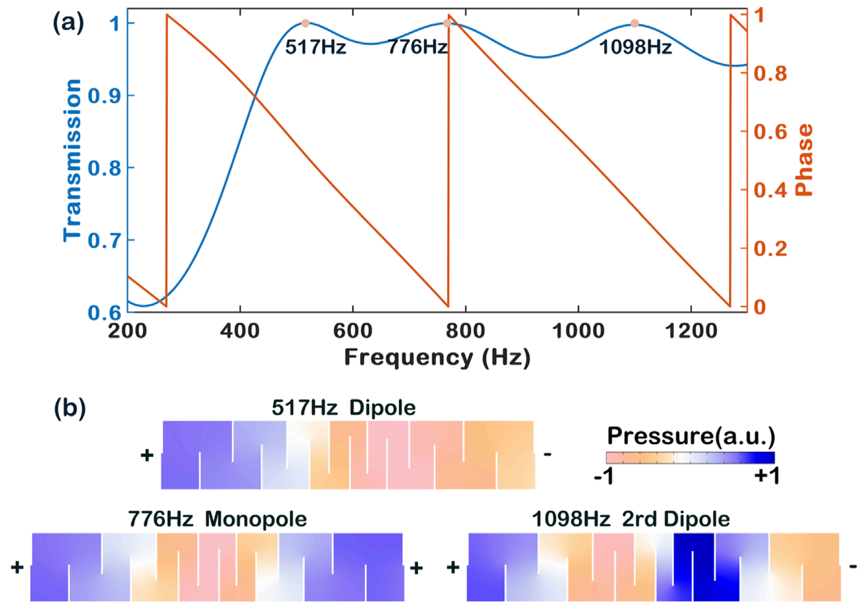

FIGURE 2
(a) Transmission and phase of the chiral coiling-space unit. **(b)** Sound-pressure distributions of the coiling-space unit at the dipole, monopole, and 2nd dipole modes.

$$p_u(x,y) = -i\rho_0 c_0 k v_{e1} \int_{-\frac{b}{2}}^{\frac{b}{2}} G_u(x,y|0,y_0)dy_0 - 2i\rho_0 c_0 k v_{v1} \int_{\frac{a}{2}-\frac{d}{2}}^{\frac{a}{2}} G_u(x,y|0,y_0)dy_0, \tag{2}$$

$$p_d(x,y) = i\rho_0 c_0 k v_{e2} \int_{-b/2}^{b/2} G_d(x,y|L,y_0)dy_0 + 2i\rho_0 c_0 k v_{v2} \int_{a/2-d/2}^{a/2} G_d(x,y|L,y_0)dy_0. \tag{3}$$

10.3389/fphy.2025.1586858

The average pressure fields at the inlet and outlet of the effective and ventilation channels, which are presented sequentially in Equations 4–7

$$P_{e1} = 2P_i - \rho_0 c_0 \{\sigma_e \upsilon_{e1}(1 + i\delta_{ee}) + \sigma_{\mathrm{v}} \upsilon_{\mathrm{v}1}(1 + i\delta_{e\mathrm{v}})\} = A_e + B_e e^{-ik_e L}, \tag{4}$$

$$P_{e2} = \rho_0 c_0 \{\sigma_e \upsilon_{e2}(1 + i\delta_{ee}) + \sigma_{\mathrm{v}} \upsilon_{\mathrm{v}2}(1 + i\delta_{e\mathrm{v}})\} = A_e e^{-ik_e L} + B_e, \tag{5}$$

$$P_{\mathrm{v}1} = 2P_i - \rho_0 c_0 \{\sigma_e \upsilon_{e1}(1 + i\delta_{e\mathrm{v}}) + \sigma_{\mathrm{v}} \upsilon_{\mathrm{v}1}(1 + i\delta_{\mathrm{vv}})\} = A_{\mathrm{v}} + B_{\mathrm{v}} e^{-ikL}, \tag{6}$$

$$P_{\mathrm{v}2} = \rho_0 c_0 \{\sigma_e \upsilon_{e2}(1 + i\delta_{\mathrm{v}e}) + \sigma_{\mathrm{v}} \upsilon_{\mathrm{v}2}(1 + i\delta_{\mathrm{vv}})\} = A_{\mathrm{v}} e^{-ikL} + B_{\mathrm{v}}, \tag{7}$$

Considering the channels are deep-subwavelength, the pressure field inside the channels can be estimated by the fundamental mode,

$$p_e(x) = A_e e^{-ik_e x} + B_e e^{ik_e(x-L)} \tag{8}$$

$$p_{\mathrm{v}}(x) = A_{\mathrm{v}} e^{-ikx} + B_{\mathrm{v}} e^{ik(x-L)} \tag{9}$$

where $A_e = \rho_e c_e \frac{\upsilon_{e1} - \vartheta_e \upsilon_{e2}}{1-\vartheta_e^2}, B_e = \rho_e c_e \frac{\vartheta_e \upsilon_{e1} - \upsilon_{e2}}{1-\vartheta_e^2}, A_{\mathrm{v}} = \rho_0 c_0 \frac{\upsilon_{\mathrm{v}1} - \vartheta \upsilon_{\mathrm{v}2}}{1-\vartheta^2}$, and $B_{\mathrm{v}} = \rho_0 c_0 \frac{\vartheta \upsilon_{\mathrm{v}1} - \upsilon_{\mathrm{v}2}}{1-\vartheta^2}$.

Substituting Equations 8, 9 into Equations (1–3) leads to the following set of equations in a matrix form for determining the normalized volume velocities at the inlet/outlet of the channels which is labeled as Equation 10:

$$\begin{bmatrix} 1 - i\left(\frac{z_e}{\sigma_e \tan \alpha_e} - \delta_{ee}\right) & i\frac{z_e}{\sigma_e \sin \alpha_e} & 1 + i\delta_{e\mathrm{v}} & 0 \\ i\frac{z_e}{\sigma_e \sin \alpha_e} & 1 - i\left(\frac{z_e}{\sigma_e \tan \alpha_e} - \delta_{ee}\right) & 0 & 1 + i\delta_{e\mathrm{v}} \\ 1 + i\delta_{e\mathrm{v}} & 0 & 1 - i\left(\frac{1}{\sigma_{\mathrm{v}} \tan \alpha} - \delta_{\mathrm{vv}}\right) & i\frac{1}{\sigma_{\mathrm{v}} \sin \alpha} \\ 0 & 1 + i\delta_{e\mathrm{v}} & i\frac{1}{\sigma_{\mathrm{v}} \sin \alpha} & 1 - i\left(\frac{1}{\sigma_{\mathrm{v}} \tan \alpha} - \delta_{\mathrm{vv}}\right) \end{bmatrix} \begin{bmatrix} \overline{\upsilon}_{e1} \\ \overline{\upsilon}_{e2} \\ \overline{\upsilon}_{v1} \\ \overline{\upsilon}_{v2} \end{bmatrix} = \begin{bmatrix} 2 \\ 0 \\ 2 \\ 0 \end{bmatrix} \tag{10}$$

where $z_e = \frac{\rho_e c_e}{\rho_0 c_0}$, the normalized volume velocities $\overline{\upsilon}_{e1}, \overline{\upsilon}_{e2}, \overline{\upsilon}_{v2}$, and $\overline{\upsilon}_{v2}$ are defined by $\overline{\upsilon} = \sigma \rho_0 c_0 v / P_i$ with σ being the open ratio of the corresponding channels.

The transmission and reflection fields are estimated from Equation 1 by considering $|x| \to \infty$, which are labelled as Equations 11, 12

$$p_t(x) = P_i(\overline{\upsilon}_{e2} + \overline{\upsilon}_{\mathrm{v}2}) e^{-ik(x-L)}, \tag{11}$$

$$p_r(x) = P_i(1 - \overline{\upsilon}_{e1} - \overline{\upsilon}_{\mathrm{v}1}) e^{ikx}, \tag{12}$$

respectively. As a result, the transmission and reflection coefficients are readily obtained as Equation 13

$$T = \overline{\upsilon}_{e2} + \overline{\upsilon}_{\mathrm{v}2} \quad \text{and} \quad R = 1 - \overline{\upsilon}_{e1} - \overline{\upsilon}_{\mathrm{v}1} \tag{13}$$

To demonstrate the broadband insulating performance of CMFRs, we judiciously choose an effective unit cell with h_1 = 37.22 mm, h_2 = 37.22 mm, w_1 = 20 mm, p = 1.11, N = 9. ρ_e/ρ_0 and c_0/c_e can be obtained using a retrieval method as 1.961 and 2.045, which have been investigated theoretically and numerically. As illustrated in Figure 3a, excellent agreement between the analytical and numerical transmission spectra, proving the correctness of the theoretical model. Here, two asymmetrical profiles of transmission peaks and three transmission dips of the unit are clearly observed, where the broadband low-transmission region can be formulated between the two transmission peaks. The coupling between the space-coiling channel and open channel induces resonance and anti-resonance. Since the former is much stronger than the latter, the induced resonance and anti-resonance are located in the close vicinity of the local resonances of the space-coiling channel. Therefore, the mode shape of the transmission dips is mainly characterized by the mode shapes of the space-coiling channel local resonances in Figure 2. It is noteworthy that the distributions of the resonances and anti-resonances for the monopolar and 2nd monopolar modes are in the opposite order and the resonance for the dipole mode is suppressed due the occurrence of consecutive anti-resonances modes. Therefore, the proper superposition of the consecutive triple Fano resonances realize a broadband sound insulating spectrum.

The broadband sound attenuation from another point of view, can be considered as the weakly coupling between the discrete resonant and continuum states. To quantitatively interpret the coupling, we further plot the phase and magnitude of $\overline{\upsilon}$ at the two channel outlets in Figure 3b. The transmission peaks occur when $\overline{\upsilon}_{e1} + \overline{\upsilon}_{\mathrm{v}1} = 1$ or $|\overline{\upsilon}_{e2} + \overline{\upsilon}_{\mathrm{v}2}| = 1$, i.e., the total volume velocity transmitted through the inlets is equal to the incident volume velocity, which obviously refers to the acoustic impedance matching condition. By contrast, the transmission reaches a minimum when the condition for transmission dips reach $\overline{\upsilon}_{e2} + \overline{\upsilon}_{\mathrm{v}2} = 0$, which indicates that the normalized volume velocities at the outlets of ventilation and the effective channels are identical in amplitude, but are out of phase. Additionally, in the middle range among the transmission dips, the phase difference between $\overline{\upsilon}_{e2}$ and $\overline{\upsilon}_{\mathrm{v}2}$ is nearly constant (π) in the region while their amplitudes show small difference. Therefore, high-quality destructive interference in the region can be expected. In this case, the broadband destructive interference can be excited in the effective coupling unit, blocking the incoming sound waves in the targeted wide frequency range.

To vividly illustrate the sound reduction performance enabled by the proposed barrier design, we present the representative numerical simulation results depicting the distributions of sound pressure and particle velocity streamlines in Figure 3c. At the transmission peak frequencies (such as 420 Hz), complete acoustic transmission can be observed on the output side. However, at the transmission dip frequencies (500 Hz, 730 Hz, and 860 Hz), total reflection occurs at the input side of the metamaterial, resulting in nearly zero energy transmission. The simulated sound field patterns reveal interference fringes on the output side, arising from the superposition of acoustic waves propagating through the helical channel and the central channel. Notably, at the intermediate weak peak frequencies of 600 Hz, a remarkably diminished amplitude is observed, indicating consistent and effective sound blocking across the entire middle frequency range.

To investigate the air permeability of the proposed barrier, we employ both laminar and turbulent flow simulations to model the air flow through the structure, which are illustrated in Figure 3d. The distinction between the laminar and turbulent flow models lies in the Reynolds number, which represents the ratio of inertial forces to viscous forces within the fluid flow. For the laminar flow model, the Reynolds number is set to 100, while for the turbulent flow model, the Reynolds number is set to 4,000. These values are chosen to represent typical flow regimes where the

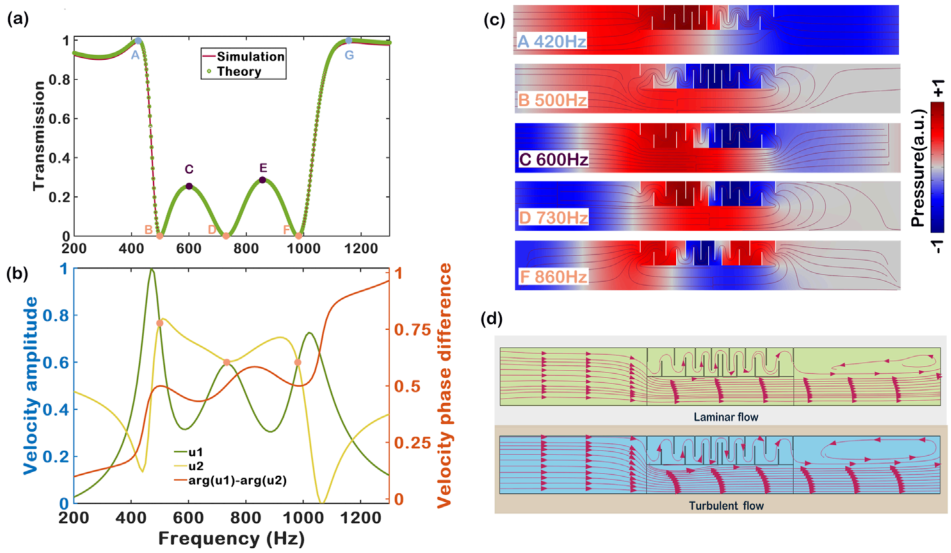

FIGURE 3
(a) Theoretically predicted and numerically calculated transmission of Fano resonant profile. **(b)** The amplitude spectra of the normalized volume velocities *u* at the outlet of the channels are shown with olive and purple lines, respectively. The phase differences of the volume velocities are also shown with the orange line corresponding to the rightward y-axis. **(c)** Simulated sound-field distributions at peak, middle weak-peak and three dips, where the white lines represent the local velocity streamlines, and the color maps illustrate the acoustic pressure distributions. **(d)** Numerical analysis results of Laminar and turbulent flow for the ventilation barrier.

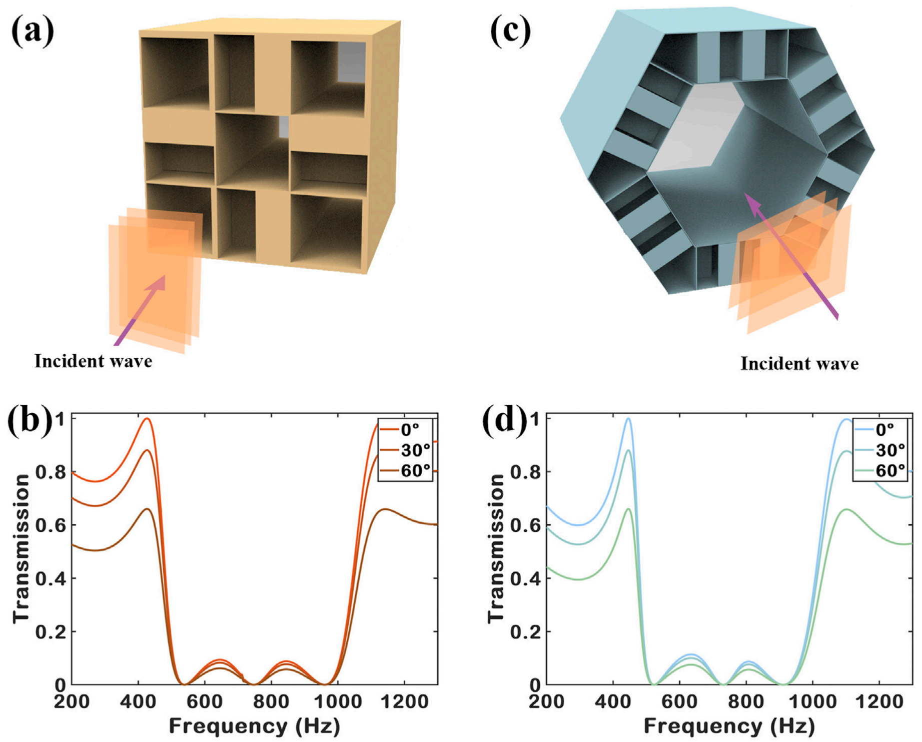

FIGURE 4
(a,b) Schematic of the 3D acoustic barrier with quadrilateral configuration based on the proposed units and numerically obtained transmission spectrum. **(c,d)** Schematic of the 3D acoustic barrier with hexagonal configuration based on the proposed units and numerically obtained transmission spectrum.

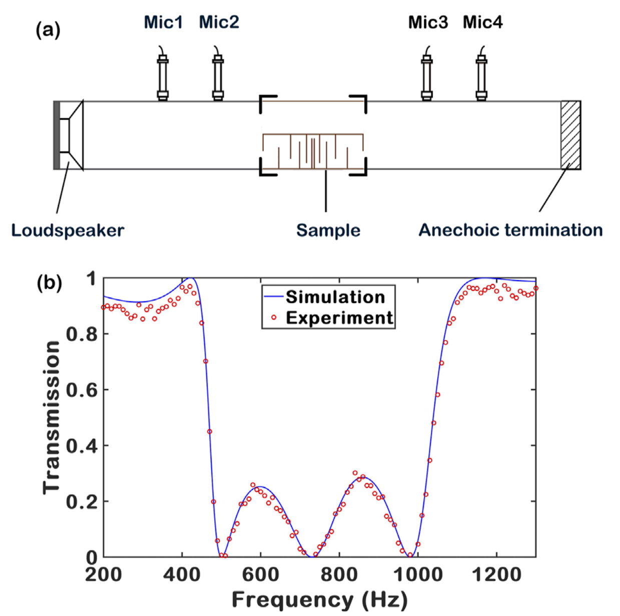

FIGURE 5
(a) Schematics of the experimental setup. **(b)** The frequency dependences on measured and simulated transmission coefficients.

fluid experiences a balance between inertial and viscous forces. The boundary conditions are set to no-slip at the walls, ensuring that the fluid velocity at the walls is zero. The simulation results demonstrate that the barrier design exhibits excellent ventilation performance under both flow regimes. Air can freely flow through the coiling-space and open channels. The key difference is that in the laminar flow scenario, only minor vortices form at the exit of the coiling-space, whereas in the turbulent flow case, with higher flow velocities, more pronounced vortex shedding occurs at the same location. It is noteworthy that despite laminar or turbulent flows, the proposed barrier architecture exhibits a remarkable ability to facilitate efficient airflow transmission, which contribute to the simultaneous realization of sound attenuation and ventilation functionalities.

In practical noise control scenarios, the complexity of the environment and the presence of various boundary constraints pose significant challenges for achieving efficient broadband noise insulation while maintaining adequate air permeability. Thanks to the flexibility and versatility, we further investigate the performance of the ACMFRs-based sound barrier in various geometrical configurations (Figures 4a,c), including hexagonal and square arrangements. As show in Figures 4b,d, we can observe that these configurations consistently maintain almost 80% noise insulation bandwidth, highly consistent with the unit case, demonstrating the robustness this mechanism. Additionally, we investigated the oblique incidence transmission characteristics of the aforementioned barrier configurations. Owing to their subwavelength features and structural symmetry, these barriers exhibit exceptional angle-insensitivity, maintaining outstanding noise attenuation even at large incidence angles. Considering various geometric configurations and incident angles, the CMFRs mechanism demonstrating superior robustness in achieving broadband noise attenuation and high air permeability, laying a solid foundation for its implementation in practical noise control scenarios such as industrial production and architectural environments.

The experiment is conducted to verify broadband silencing performance of the proposed enhanced Fano-type acoustic silencer. In our experiments, as depicted in Figure 5a, we set up a test environment to measure the transmission coefficients across a range of frequencies. The sound transmission coefficients of a 3D-printed sample are measured in the laboratory-made impedance tube, utilizing the four-load method. The results, shown in Figure 5b alongside the numerical predictions, reveal a strong correlation between the experimental and simulated data. This congruence underscores the effectiveness of our design in blocking incident waves across a broad frequency band. However, we did observe that the experimental transmission spectrum is marginally lower than the numerical predictions. We attribute these discrepancies primarily to two factors: first, the weak absorption caused by viscous energy dissipation within the material, which was not accounted for in our simulations; and second, discrepancies arising from sample fabrication errors. These factors can introduce variability and deviations in the actual performance compared to the idealized model.

In conclusion, we have theoretically proposed and demonstrated a low-frequency acoustic chiral barrier that achieves consecutive multiple Fano resonances for simultaneous broadband noise reduction and ventilation. The barrier unit composed of chiral space-coiling tunnel and hollow pipes supports the broadband weakly coupling between the discrete resonant and continuum states. Through judiciously tuning the coupling of above two states, multiple order Fano resonances generate broadband sound attenuation in the range of 479–1,032 Hz. Good agreement between the simulated, theoretical, and experimental results validate the broadband sound reduction over this frequency range. Notably, the flow simulations indicate that the Fano-based barrier can maintain an efficient airflow transmission, presenting a highly ventilated noise reduction solution. This work realizes a flexible, ventilated, and broadband noise barrier using consecutive Fano resonances, enabling low-frequency airborne sound insulation under ventilation.

Data availability statement

The raw data supporting the conclusions of this article will be made available by the authors, without undue reservation.

Author contributions

Z-xX: Data curation, Investigation, Software, Validation, Writing – original draft. YF: Conceptualization, Project administration, Resources, Supervision, Writing – review and editing. X-pW: Project administration, Resources, Supervision, Writing – review and editing.

Funding

The author(s) declare that no financial support was received for the research and/or publication of this article.

Conflict of interest

The authors declare that the research was conducted in the absence of any commercial or financial relationships that could be construed as a potential conflict of interest.

Generative AI statement

The author(s) declare that no Generative AI was used in the creation of this manuscript.

Publisher's note

All claims expressed in this article are solely those of the authors and do not necessarily represent those of their affiliated organizations, or those of the publisher, the editors and the reviewers. Any product that may be evaluated in this article, or claim that may be made by its manufacturer, is not guaranteed or endorsed by the publisher.

References

1. Dong R, Sun M, Mo F, Mao D, Wang X, Li Y. Recent advances in acoustic ventilation barriers. *J Phys D: Appl Phys* (2021) 54:403002. doi:10.1088/1361-6463/ac1228

2. Ma G, Yang M, Xiao S, Yang Z, Sheng P. Acoustic metasurface with hybrid resonances. *Nat Mater* (2014) 13:873–8. doi:10.1038/nmat3994

3. Xu Z-x., Gao H, Ding Y-j., Yang J, Liang B, Cheng J-c. Topology-optimized omnidirectional broadband acoustic ventilation barrier. *Phys Rev Appl* (2020) 14:054016.

4. Attaran A, Emami SD, Soltanian MRK, Penny R, Behbahani F, Harun SW, et al. Circuit model of Fano resonance on tetramers, pentamers, and broken symmetry pentamers. *Plasmonics* (2014) 9:1303–13. doi:10.1007/s11468-014-9743-y

5. Bärnthaler A, Rotter S, Libisch F, Burgdörfer J, Gehler S, Kuhl U, et al. Probing decoherence through Fano resonances. *Phys Rev Lett* (2010) 105(4):056801. doi:10.1103/physrevlett.105.056801

6. Fan PY, Yu ZF, Fan SH, Brongersma ML. Optical Fano resonance of an individual semiconductor nanostructure. *Nat Mater* (2014) 13:471–5. doi:10.1038/nmat3927

7. Fano U. Effects Of Configuration Interaction On Intensities And Phase Shifts. *Phys Rev* (1961) 124:1866–78. doi:10.1103/physrev.124.1866

8. Johnson AC, Marcus CM, Hanson MP, Gossard AC. Coulomb-modified Fano resonance in a one-lead quantum dot. *Phys Rev Lett* (2004) 93(4):106803. doi:10.1103/physrevlett.93.106803

9. Miroshnichenko AE, Flach S, Kivshar YS. Fano resonances in nanoscale structures. *Rev Mod Phys* (2010) 82:2257–98. doi:10.1103/revmodphys.82.2257

10. Qiang ZX, Yang HJ, Chuwongin S, Zhao DY, Ma ZQ, Zhou WD. Design of Fano broadband reflectors on SOI. *Ieee Photon Technology Lett* (2010) 22:1108–10. doi:10.1109/lpt.2010.2050471

11. Shafiei F, Monticone F, Le KQ, Liu XX, Hartseld T, Alù A, et al. A subwavelength plasmonic metamolecule exhibiting magnetic-based optical Fano resonance. *Nat Nanotechnology* (2013) 8:95–9. doi:10.1038/nnano.2012.249

12. Wang YF, Liao L, Hu T, Luo S, Wu L, Wang J, et al. Exciton-polariton Fano resonance driven by second harmonic generation. *Phys Rev Lett* (2017) 118(5):063602. doi:10.1103/physrevlett.118.063602

13. Wu CH, Khanikaev AB, Shvets G. Broadband slow light metamaterial based on a double-continuum Fano resonance. *Phys Rev Lett* (2011) 106(4):107403. doi:10.1103/physrevlett.106.107403

14. Chen Z, Fan L, Zhang SY, Zhang H, Li XJ, Ding J. An open-structure sound insulator against low-frequency and wide-band acoustic waves. *Appl Phys Express* (2015) 8(4):107301. doi:10.7567/apex.8.107301

15. Choy YS, Huang LX. Experimental studies of a drumlike silencer. *J Acoust Soc America* (2002) 112:2026–35. doi:10.1121/1.1508779

16. Dong R, Mao D, Wang X, Li Y. Ultrabroadband acoustic ventilation barriers via hybrid-functional metasurfaces. *Phys Rev Appl* (2021) 15:024044. doi:10.1103/physrevapplied.15.024044

17. Huang S, Fang X, Wang X, Assouar B, Cheng Q, Li Y. Acoustic perfect absorbers via Helmholtz resonators with embedded apertures. *J Acoust Soc Am* (2019) 145:254–62. doi:10.1121/1.5087128

18. Krasikova M, Krasikov S, Melnikov A, Baloshin Y, Marburg S, Powell DA, et al. Metahouse: noise-insulating chamber based on periodic structures. *Adv Mater Tech* (2022) 8. doi:10.1002/admt.202200711

19. Liu TW, Chan CT, Wu RT. Deep-Learning-based acoustic metamaterial design for attenuating structure-borne noise in auditory frequency bands. *Materials (Basel)* (2023) 16:1879. doi:10.3390/ma16051879

20. Meng Y, Romero-García V, Gabard G, Groby JP, Bricault C, Goudé S. Subwavelength broadband perfect absorption for unidimensional open-duct problems. *Adv Mater Tech* (2023) 8. doi:10.1002/admt.202201909

21. Tang Y, Liang B, Lin S. Broadband ventilated meta-barrier based on the synergy of mode superposition and consecutive Fano resonances. *J Acoust Soc Am* (2022) 152:2412–8. doi:10.1121/10.0014911

22. Wu H-W, Yin Y-Q, Sheng Z-Q, Li Y, Qi D-X, Peng R-W. Multiband omnidirectional ventilated acoustic barriers based on localized acoustic rainbow trapping. *Phys Rev Appl* (2021) 15:054033. doi:10.1103/physrevapplied.15.054033

23. Xiang L, Wang G, Zhu C, Shi M, Hu J, Luo G. Ventilation barrier with space-coiling channels of varying cross-section for broadband sound insulation. *Appl Acoust* (2022) 201:109110.

24. Xu ZX, Gao H, Ding YJ, Yang J, Liang B, Cheng JC. Topology-optimized omnidirectional broadband acoustic ventilation barrier. *Phys Rev Appl* (2020) 14(8):054016. doi:10.1103/physrevapplied.14.054016

25. Zhu XF, Li K, Zhang P, Zhu J, Zhang JT, Tian C, et al. Implementation of dispersion-free slow acoustic wave propagation and phase engineering with helical-structured metamaterials. *Nat Commun* (2016) 7(7):11731. doi:10.1038/ncomms11731

26. Zhu Y, Dong R, Mao D, Wang X, Li Y, Ventilating Metasurfaces N. Nonlocal ventilating metasurfaces. *Phys Rev Appl* (2023) 19:014067. doi:10.1103/physrevapplied.19.014067

27. Ghaffarivardavagh R, Nikolajczyk J, Anderson S, Zhang X. Ultra-open acoustic metamaterial silencer based on Fano-like interference. *Phys Rev B* (2019) 99(10):024302.

28. Zhang HL, Zhu YF, Liang B, Yang J, Yang J, Cheng JC. Omnidirectional ventilated acoustic barrier. *Appl Phys Lett* (2017) 111(4):203502. doi:10.1063/1.4993891

29. Limonov MF, Rybin MV, Poddubny AN, Kivshar YS. Fano resonances in photonics. *Nat Photon* (2017) 11:543–54. doi:10.1038/nphoton.2017.142

30. Xu Z-x., Qiu W-j., Cheng Z-q., Yang J, Liang B, Cheng J-c. Broadband ventilated sound insulation based on acoustic consecutive multiple Fano resonances. *Phys Rev Appl* (2024) 21:044049. doi:10.1103/physrevapplied.21.044049

31. Nguyen HQ, Wu Q, Chen H, Chen JJ, Yu YK, Tracy S, et al. A Fano-based acoustic metamaterial for ultra-broadband sound barriers. *Proc R Soc A: Math Phys Eng Sci* (2021) 477. doi:10.1098/rspa.2021.0024

32. Shi J, Liu C, Liu X, Lai Y. Ventilative meta-window with broadband low-frequency acoustic insulation. *J Appl Phys* (2021) 129. doi:10.1063/5.0042384

33. Sun M, Fang X, Mao D, Wang X, Li Y. Broadband acoustic ventilation barriers. *Phys Rev Appl* (2020) 13:044028. doi:10.1103/physrevapplied.13.044028

34. Wu H, Zhang H, Hao C. Reconfigurable spiral underwater sound-absorbing metasurfaces. *Extreme Mech Lett* (2021) 47:101361. doi:10.1016/j.eml.2021.101361

35. Xiang L, Wang G, Zhu C, Shi M, Hu J, Luo G. Ventilation barrier with space-coiling channels of varying cross-section for broadband sound insulation. *Appl Acoust* (2022) 201:109110. doi:10.1016/j.apacoust.2022.109110

36. Xu Z-x., Zheng B, Yang J, Liang B, Cheng J-c. Machine-learning-assisted acoustic consecutive Fano resonances: application to a tunable broadband low-frequency metasilencer. *Phys Rev Appl* (2021) 16:044020. doi:10.1103/physrevapplied.16.044020

37. Liu C, Shi J, Zhao W, Zhou X, Ma C, Peng R, et al. Three-dimensional soundproof acoustic metacage. *Phys Rev Lett* (2021) 127:084301. doi:10.1103/physrevlett.127.084301

38. Liang ZX, Li JS. Extreme acoustic metamaterial by coiling up space. *Phys Rev Lett* (2012) 108(4):114301. doi:10.1103/physrevlett.108.114301

39. Kumar S, Lee HP. Labyrinthine acoustic metastructures enabling broadband sound absorption and ventilation. *Appl Phys Lett* (2020) 116. doi:10.1063/5.0004520

40. Li Y, Qi S, Assouar MB. Theory of metascreen-based acoustic passive phased array. *New J Phys* (2016) 18:043024. doi:10.1088/1367-2630/18/4/043024

41. Ghaffarivardavagh R, Nikolajczyk J, Anderson S, Zhang X. Ultra-open acoustic metamaterial silencer based on Fano-like interference. *Phys Rev B* (2019) 99:024302. doi:10.1103/physrevb.99.024302